Spatial Optimal Interpolation of *Aquarius* Sea Surface Salinity: Algorithms and Implementation in the North Atlantic*

OLEG MELNICHENKO

International Pacific Research Center, School of Ocean and Earth Science and Technology, University of Hawai'i at Mānoa, Honolulu, Hawaii

PETER HACKER

Hawaii Institute of Geophysics and Planetology, School of Ocean and Earth Science and Technology, University of Hawai'i at Mānoa, Honolulu, Hawaii

NIKOLAI MAXIMENKO

International Pacific Research Center, School of Ocean and Earth Science and Technology, University of Hawai'i at Mānoa, Honolulu, Hawaii

GARY LAGERLOEF

Earth and Space Research, Seattle, Washington

JAMES POTEMRA

Hawaii Institute of Geophysics and Planetology, School of Ocean and Earth Science and Technology, University of Hawai'i at Mānoa, Honolulu, Hawaii

(Manuscript received 1 November 2013, in final form 5 March 2014)

ABSTRACT

A method is presented for mapping sea surface salinity (SSS) from *Aquarius* level-2 along-track data in order to improve the utility of the SSS fields at short length [O(150 km)] and time [O(1 week)] scales. The method is based on optimal interpolation (OI) and derives an SSS estimate at a grid point as a weighted sum of nearby satellite observations. The weights are optimized to minimize the estimation error variance. As an initial demonstration, the method is applied to *Aquarius* data in the North Atlantic. The key element of the method is that it takes into account the so-called long-wavelength errors (by analogy with altimeter applications), referred to here as interbeam and ascending/descending biases, which appear to correlate over long distances along the satellite tracks. The developed technique also includes filtering of along-track SSS data prior to OI and the use of realistic correlation scales of mesoscale SSS anomalies. All these features are shown to result in more accurate SSS maps, free from spurious structures. A trial SSS analysis is produced in the North Atlantic on a uniform grid with 0.25° resolution and a temporal resolution of one week, encompassing the period from September 2011 through August 2013. A brief statistical description, based on the comparison between SSS maps and concurrent in situ data, is used to demonstrate the utility of the OI analysis and the potential of *Aquarius* SSS products to document salinity structure at ~150-km length and weekly time scales.

1. Introduction

Sea surface salinity (SSS) is a key parameter that reflects the intensity of the marine hydrological cycle (U.S. CLIVAR Office 2007). *Aquarius/Satelite de Aplicaciones Cientificas-D* (*SAC-D*) satellite observations provide an opportunity to observe near-global SSS with space and time resolution not available by other components of the Global Ocean Observing System (GOOS).

* School of Ocean and Earth Science and Technology Contribution Number 9105 and International Pacific Research Center Contribution Number 1052.

Corresponding author address: Oleg Melnichenko, International Pacific Research Center, University of Hawai'i at Mānoa, POST Bldg., Room 401, 1680 East-West Road, Honolulu, HI 96822.
E-mail: oleg@hawaii.edu

DOI: 10.1175/JTECH-D-13-00241.1

© 2014 American Meteorological Society

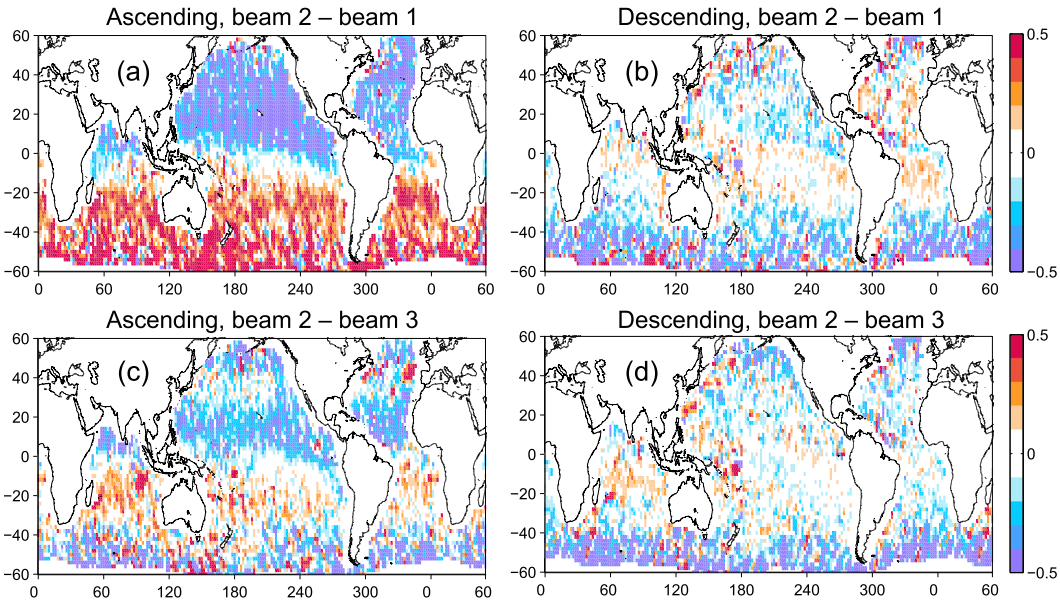

FIG. 1. Global maps of interbeam SSS differences (psu) averaged over September 2012. (top) SSS of beam 2 (middle beam) minus SSS of beam 1 for (a) ascending and (b) descending satellite passes. (bottom) SSS of beam 2 minus SSS of beam 3 for (c) ascending and (d) descending satellite passes. Areas where the differences are smaller than 0.2 psu are blanked. The interbeam SSS differences are computed by differing monthly SSS fields constructed by bin averaging of raw *Aquarius* data (each beam separately) within 4° × 4° bins centered on a global grid with the grid spacing of 2° in both zonal and meridional directions.

Aquarius/SAC-D is a collaborative space mission between the National Aeronautics and Space Administration (NASA) and Argentina's space agency. Since its launch in June 2011 and the onset of data delivery in late August 2011, the *Aquarius/SAC-D* satellite has been providing space-based observations of SSS with a complete global coverage every 7 days. The satellite is positioned on a polar sun-synchronous orbit crossing the equator at 1800 local time (LT) (ascending) and 0600 LT (descending). The *Aquarius* instrument consists of three microwave radiometers that generate three beams at different angles relative to the sea surface. The beams form three elliptical footprints on the sea surface (76 km × 94 km, 84 km× 120 km, and 96 km × 156 km), aligned across a ~390-km-wide swath. The emission from the sea surface, measured by the radiometers as an equivalent brightness temperature in kelvins, is converted to SSS, subject to corrections for various geophysical effects. A detailed description of the *Aquarius/SAC-D* satellite mission and the *Aquarius* instrument can be found in Le Vine et al. (2007) and Lagerloef et al. (2008).

Since the availability of *Aquarius* on-orbit data, the calibration/validation team has been actively identifying problems and errors, improving algorithms, and updating the versions of available data. With respect to SSS, significant sources of errors are temporal sensor drift, ascending/descending biases, and interbeam biases (Lagerloef et al. 2013). The latter biases are the focus of the present study. Although there has been steady improvement in the level-2 SSS versions over the past two years, both the ascending/descending biases and interbeam biases continue to have significant space–time variability globally, and are the primary source of residual calibration errors in *Aquarius* SSS retrievals that manifest themselves as artificial north–south-striped patterns in mapped SSS fields.

Figure 1, showing global maps of interbeam differences averaged over the month of September 2012, illustrates the problem. The differences are shown separately for ascending (from southeast to northwest) and descending (from northeast to southwest) *Aquarius* passes. In many areas, the interbeam differences are much larger than 0.2 psu and do not represent the true ocean signal. Note the large-scale structure of the interbeam differences and the differences between the ascending and descending patterns. The differences also have large amplitude temporal variations with an annual cycle (not shown).

The primary objective of this investigation is to test the possibility of correcting errors in *Aquarius* SSS data by incorporating available statistical information about the signal and noise into the mapping procedure commonly known as optimal interpolation (OI). OI is a fairly straightforward but powerful method of data analysis, extensively used by oceanographers and

meteorologists for estimating values of geophysical variables on a regular grid from irregularly sampled observations. The method is based on the Gauss–Markov theorem (Gandin 1965; Bretherton et al. 1976; McIntosh 1990) and determines a pointwise estimate of the interpolated field with minimum ensemble mean-square error, given prior information about the variances and correlation functions of the estimated field and the data. The latter requirement is probably the hardest step in practical implementation of the method to the problem of mapping the *Aquarius* SSS. This is partly because in many parts of the ocean, there are insufficient high-resolution observations to confidently specify the required statistics of the field (Bingham et al. 2002). The attractive feature of OI, however, is that it affords a very convenient way of taking into account error information specific to a given observational platform. This is particularly relevant to the satellite SSS data, since errors in the satellite retrievals are of different types and are spatially correlated (Lagerloef et al. 2013). Finally, the OI formalism has been successfully applied for mapping various satellite data, such as sea surface temperature (e.g., Reynolds and Smith 1994; Reynolds et al. 2007; Thiebaux et al. 2003) and sea level anomaly (Le Traon et al. 1998; Ducet et al. 2000). Many ideas originally developed for these applications are found to be fruitful for the present study as well.

In this paper we focus on the North Atlantic between 0° and 40°N. The choice of this particular region is motivated by the ongoing field experiment Salinity Processes in the Upper Ocean Regional Study (SPURS) to study the physical processes that are responsible for the maintenance and magnitude of the subtropical Atlantic salinity maximum. The overall region includes substantial space–time variability of SSS as well as significantly enhanced near-surface, in situ salinity observations during SPURS.

The rest of the paper is organized as follows. Section 2 provides an overview of the satellite SSS data. Section 3 provides a general description of the algorithm; specifics are given in section 4. Section 5 presents results that formally validate the use of the long-wavelength error model to correct *Aquarius* SSS data for interbeam biases. An intercomparison of SSS analyses is presented in section 6. Section 7 provides the main conclusions and a brief discussion of possible improvements of the analysis.

2. *Aquarius* SSS data

In the present study, we use level-2 (L2) version 2.0 *Aquarius* data produced by the NASA Goddard Space Flight Center's Aquarius Data Processing System (ADPS). The L2 data files, distributed by the Physical Oceanography Distributed Active Archive Center (PO.DAAC) of the Jet Propulsion Laboratory (JPL), contain retrieved SSS, navigation data, ancillary fields, confidence flags, and other related information such as surface winds. The data are structured as a sequence of files, each corresponding to one orbit of *Aquarius*. An orbit is defined as starting when the satellite passes the South Pole. Individual observations along each orbit consist of a sequence of data points sampled at a 1.44-s (~10 km) interval. Each individual observation represents the average salinity in the upper 1–2-cm layer and over a ~100-km footprint (Le Vine et al. 2007; Lagerloef et al. 2008). The ancillary SSS data are provided from the global 1/12° data-assimilative Hybrid Coordinate Ocean Model (HYCOM). The model assimilates satellite altimeter observations, satellite, and in situ SST as well as vertical temperature/salinity profiles from Argo floats and moored buoys. More details on HYCOM can be found in Chassignet et al. (2009). In *Aquarius* L2 data files, the HYCOM SSS is interpolated to the time and location of every *Aquarius* 1.44-s sample interval (Lagerloef et al. 2013).

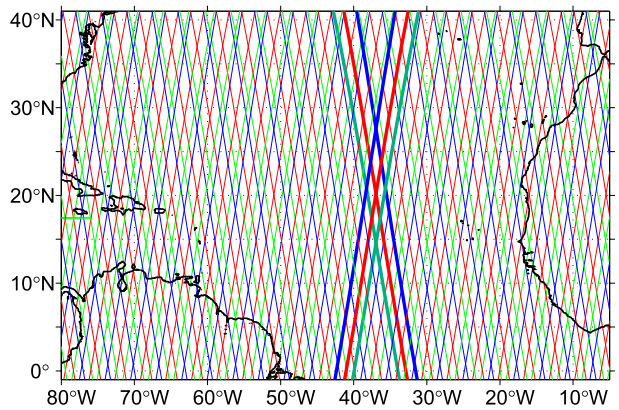

FIG. 2. Example pattern of *Aquarius* ground tracks over the North Atlantic over a 7-day period. Colors indicate the three *Aquarius* beams. Ascending passes are from southeast to northwest. Heavy lines (green, red, and blue) indicate two swaths (ascending and descending) passing through the SPURS site (25°N, 38°W).

Figure 2 shows the *Aquarius* ground tracks over the North Atlantic between the equator and 40°N. Each track represents three radiometer beams shown by different colors. The *Aquarius* sampling pattern is quite dense, implying that a variety of commonly used interpolation techniques can be applied to construct a spatially mapped product. The problem, however, lies in the relatively large retrieval errors in the satellite SSS data, which, if not corrected, result in spurious structures in the corresponding SSS maps.

An example of L2 SSS data is shown in Fig. 3, illustrating that there are at least two types of errors in the

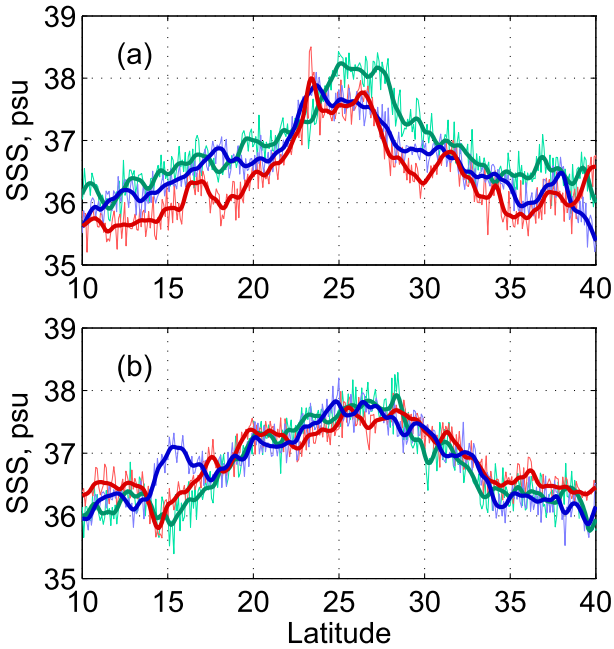

FIG. 3. Examples of along-track SSS (three beams, 390-km-wide swath): (a) ascending, passing through the North Atlantic on 14 September 2012; and (b) descending, passing through the North Atlantic on 11 Sep 2012 (see Fig. 2 for locations). Thin curves—raw data; thick curves—smoothed with a running Hanning filter of half-width of ~60 km (approximately half-width of the *Aquarius* footprint). Colors indicate the three *Aquarius* beams.

SSS retrievals. A significant source of error is the accuracy of individual measurements along the satellite tracks. An important aspect of this error is its random character and a very short wavelength. As will be shown later, this short-wavelength noise is essentially "white" in nature and can effectively be suppressed by averaging over a sufficient number of observations or by filtering the data along track, such as shown in Fig. 3 (heavy lines).

Of much greater concern are differences between the three beams, which can be as large as 0.5–0.8 psu and appear to be correlated over large distances along the satellite tracks. This type of error is also illustrated by Fig. 3. During the satellite pass over the North Atlantic on 14 September 2012, the middle beam (red) delivered systematically lower SSS as compared to the other two beams. Such interbeam biases are likely a manifestation of residual geophysical corrections. Since the three radiometer beams view the ocean surface at slightly different angles, each beam is affected by geophysical errors differently (Lagerloef et al. 2013).

3. Interpolation procedure

In the interpolation procedure, it is desirable not only to extract all available information from the satellite data but to simultaneously correct for various errors. The ultimate goal is to produce the best possible estimate of the evenly gridded SSS field. The OI analysis attempts to accomplish this goal by minimizing the mean-square interpolation error for an ensemble of analysis realizations (Gandin 1965; Bretherton et al. 1976).

a. General description of algorithm

The interpolation expression for OI with N observations can be written as (Bretherton et al. 1976; McIntosh 1990; Le Traon et al. 1998)

$$\hat{S}_x = S_x^0 + \sum_{i=1}^{N}\sum_{j=1}^{N} A_{ij}^{-1} C_{xj}(S_i^{\mathrm{obs}} - S_i^0), \tag{1}$$

where $\hat{S}_x$ is the interpolated value (or estimate) at the grid point $\mathbf{x}$, S_x^0 is the forecast (or "first guess") value at the grid point $\mathbf{x}$, S_i^{obs} is the measured value at the observation point i, S_i^0 is the forecast value at the observation point i, $\mathbf{A}$ is the $N \times N$ covariance matrix of the data

$$A_{ij} = \langle (S_i^{\mathrm{obs}} - S_i^0)(S_j^{\mathrm{obs}} - S_j^0) \rangle, \tag{2}$$

and $\mathbf{C}$ is the joint covariance matrix of the data and the field to be estimated, where

$$C_{xj} = \langle (S_x - S_x^0)(S_j^{\mathrm{obs}} - S_j^0) \rangle. \tag{3}$$

It is generally assumed that the field S_i is imperfectly measured at observation points, yielding values with random errors ε_i: $S_i^{\mathrm{obs}} = S_i + \varepsilon_i$. It is also assumed, as is usually reasonable, that the errors and the field are not correlated. Then the general elements of the covariance matrices (2) and (3) can be written as

$$A_{ij} = \langle (S_i - S_i^0)(S_j - S_j^0) \rangle + \langle \varepsilon_i \varepsilon_j \rangle, \tag{4}$$

$$C_{xj} = \langle (S_x - S_x^0)(S_j - S_j^0) \rangle. \tag{5}$$

The analysis is determined relative to the "first guess" field, which is assumed to be a good approximation of the true state. The estimate and the observations are then equal to the first guess plus small increments. In this way, the gridpoint analysis consists of interpolation of the first-guess field to the observation points followed by interpolation of the differences between the observed and first-guess values back to the grid point according to (1).

The following a priori information is required for construction of a successful OI scheme:

- A background or first-guess field with location-dependent values S_x^0, which may be a field of climatological means or continually updated running averages

or forecasts (e.g., Clancy et al. 1990; Reynolds and Smith 1994).

- Covariance of the field to be analyzed. In practice, it is often expressed in a simple analytical form with a few degrees of freedom, allowing for a practical estimation of parameters from observations.
- Covariance of the measurement noise, which can be estimated from an ensemble of realizations of the data, in particular, from a long time series of the data.

Specific choices of parameters used to construct gridded SSS fields from *Aquarius* L2 data in the North Atlantic are addressed in the following section.

b. Specifics

1) PREPARATION OF INPUT DATA

To produce the gridded product, the L2 SSS data are first checked for quality. Data points contaminated by land (land fraction > 0.005) are excluded from the analysis. Also excluded from the analysis are data points that are flagged as severely contaminated by radio frequency interference (RFI), and/or sampled during high wind (wind speed $> 15\,\mathrm{m\,s^{-1}}$).

The next step consists of smoothing the along-track SSS data (each beam separately) with a running Hanning filter of half-width of about 60 km to suppress high-frequency instrument noise (e.g., Fig. 3). With the *Aquarius* ~10-km along-track sampling, the filter weights 12 adjacent observations, which has been found to be quite sufficient to significantly reduce the noise level, yet preserve the ocean signal from oversmoothing.

The effect of filtering of the along-track data is demonstrated in Fig. 4, which displays the mean wavenumber spectra of SSS representing the unfiltered and filtered data from the *Aquarius* repeat track passing through the North Atlantic (see Fig. 2 for location). The spectrum of the unfiltered data (blue line) is characterized by a pronounced transition from "red" to "white" shape at the wavelength near 100 km. The white spectrum at wavelengths shorter than 100 km is primarily due to the instrument noise. At wavelengths longer than 100 km, the oceanic signal starts to emerge and the power level rises toward the longest wavelength resolved by the spectral analysis. Integrating the power of the white noise over the wavenumber domain yields a root-mean-square error of ~0.21 psu. The signal-to-noise ratio, defined as the ratio of the low-wavenumber signal variance to the high-wavenumber noise variance, is about 40 at 1000-km wavelength and only 10 at 500-km wavelength. After applying the filter procedure (red line) most of the short-wavelength noise is eliminated while leaving the ocean signal practically unchanged. [this can be shown, e.g., by subtracting a flat variance of white noise (0.00025 psu^2) from the blue curve; the result is the green curve]. It is likely, however, that residual noise effects are still present in the filtered data, particularly in the form of long-wavelength errors, which are treated separately.

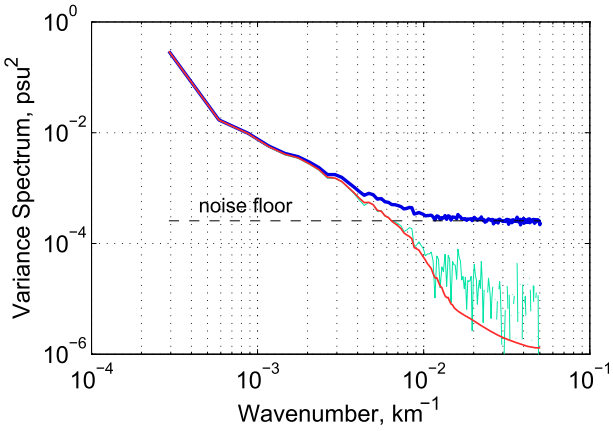

FIG. 4. Mean along-track wavenumber spectra of SSS in the area between 10° and 40°N computed from the data of the ascending portion of the *Aquarius* repeat swath that passes through the SPURS domain (see Fig. 2 for location). The spectra are computed from 83 *Aquarius* passes (September 2011–April 2013) and the three beams are averaged together. The blue and red curves represent the unfiltered and filtered data, respectively, as described in the text. The total variances associated with the blue and red curves are 0.396 and 0.352 psu^2, respectively. The green curve is obtained by subtracting a flat variance of white noise (0.00025 psu^2; black dashed line) from the blue curve.

2) FIRST GUESS

The first-guess fields, from which deviations are computed by the OI analysis, are derived from monthly-mean SSS fields obtained with variational interpolation of Argo buoy measurements. The Argo product is developed at the Asia-Pacific Data-Research Center (APDRC), which provides salinity maps on standard depth levels on a monthly basis (http://apdrc.soest.hawaii.edu/projects/argo/). Figure 5 shows an example of the Argo-derived monthly-mean SSS field in the North Atlantic.

The advantage of using Argo-derived SSS fields as the first guess is twofold. First, Argo-derived SSS fields are independent of the analysis of the satellite data. Therefore, the data increments, defined as the difference between the data and the first guess, are also independent of the analysis and can be used to compute the error statistics required by OI (Reynolds and Smith 1994). Second, Argo-derived SSS fields, since they are based on concurrent data, provide unbiased estimates of the first guess as compared to, say, climatological fields, which can be biased at large-scales due to the presence

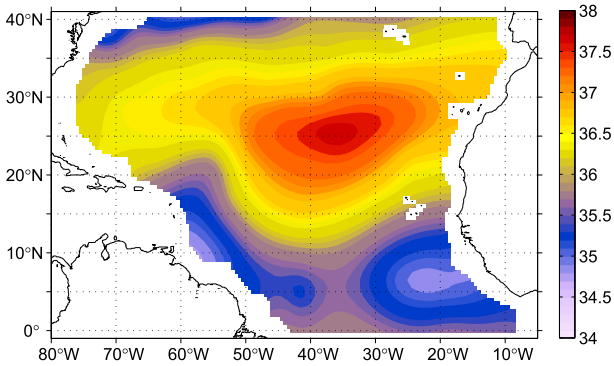

FIG. 5. September 2012 mean SSS field (psu) from in situ Argo float data (APDRC product).

of significant trends related to climate change (e.g., Durack and Wijffels 2010) and/or their reliance on highly inhomogeneous multitype-instrument historical data (Gouretski and Koltermann 2007; Roemmich and Gilson 2009).

3) SIGNAL STATISTICS

The OI analysis is determined in terms of data increments relative to a first guess. Therefore, the signal statistics, required by OI, must be derived for the data increments relative to the specified first guess (Reynolds and Smith 1994). However, the *Aquarius* along-track data are contaminated by long-wavelength correlated errors, which may result in correlation functions dominated by these errors. To overcome this problem, the spatial correlation structure of mesoscale SSS anomalies is derived from *Aquarius* data by dividing the along-track observations into shorter 10° latitude segments. The basic assumption here is that the dominant wavelengths of the correlated errors are long enough (half wavelength > 10° in latitude; Fig. 1) such that the effect of these errors can significantly be reduced by removing liner trends fitted to the along-track SSS data.

The spatial correlation scales of SSS anomalies were computed from *Aquarius* data as follows. The L2 SSS data [low-pass filtered as described in section 3b(1)] were split into four subregions, each spanning 10° in latitude: 0°–10°, 10°–20°, 20°–30°, and 30°–40°N. The first-guess values of SSS were subtracted from the data to obtain the data increments. Here, the first-guess values of SSS at observation locations at any given time were obtained by the space–time interpolation of the Argo-derived monthly-mean SSS fields [section 3b(2)]. To estimate autocorrelation functions of SSS, linear trends were first removed for each 10° ground-track segment to produce SSS anomalies, presumably free from long-wavelength errors. The along-track autocorrelation functions of SSS anomalies were then estimated for the fractions of ascending and descending paths that span individual 10° subregions, assuming that the correlation between two points on a given track is a function only of a distance between the points. Finally, the ensemble mean autocorrelation functions in each subregion were estimated by averaging over all the corresponding individual autocorrelations.

Figure 6 illustrates the procedure described above. Displayed are ensemble-mean autocorrelations of SSS for the repeat swath shown by the heavy lines in Fig. 2. Each color in Fig. 6 represents a group of ground-track segments within a particular latitude band. For comparison, autocorrelation functions of ancillary SSS are shown by the dashed lines. [The model-derived L2 ancillary data were processed in exactly the same way as *Aquarius* data (including along-track filtering) except for replacing the first guess by the time mean over the period of *Aquarius* observations.] The space-lagged correlations computed from the *Aquarius* along-track data agree well with the correlations computed from ancillary SSS, providing additional confidence in our approach. Note that ancillary SSS, since it comes from a HYCOM model solution, is free from "measurement" errors, including long-wavelength errors.

Figure 6 indicates that the structure of the correlation functions is very similar in all latitude bands. The spatial (meridional) scales of mesoscale SSS variability, determined here as the lag of the first zero crossing of the corresponding correlation function, vary little with latitude. They are ~180 km in the zonal band 0°–10°N and ~150 km in the zonal band 30°–40°N. Because the differences are relatively small, it is reasonable to model SSS variability with a constant spatial decorrelation scale, independent of latitude (see also Table 1). To approximate the observed correlation array, we choose to use a simple Gaussian curve given by

$$c(r) = \exp(-r^2/R^2), \tag{6}$$

where r is the spatial lag and $R = 90$ km is the e-folding decay scale.

The Gaussian function with the e-folding scale $R = 90$ km (green curve in Fig. 6a) was found to best represent the shape of the ensemble-mean autocorrelation function over the distance range 0–180 km. The corresponding wavenumber spectra are displayed in Fig. 6b. In the wavelength range from about 60 to 300 km, the empirical spectrum follows a power law of the form $\sim k^{-2}$, where k is the wavenumber. Note that the Gaussian-shape autocorrelation function has the decay rate for k that matches that of the observed spectra.

The apparent shortcoming of the Gaussian function, which we select as a statistical model for interpolation of

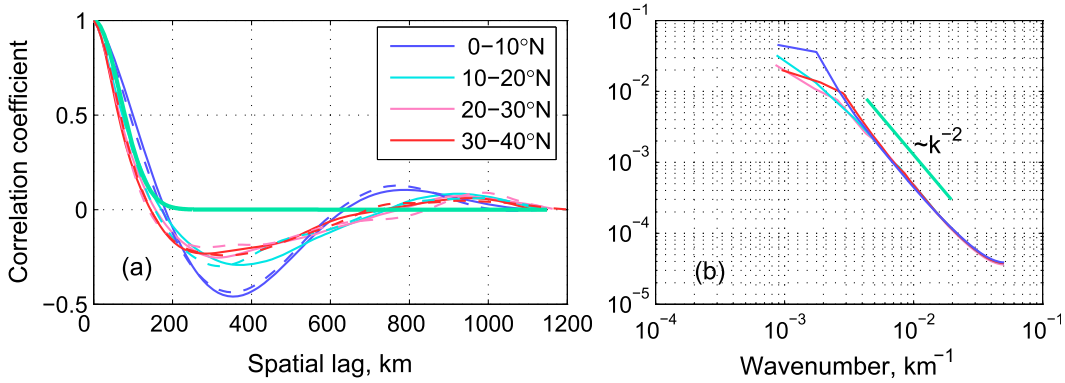

FIG. 6. (a) Autocorrelation functions for SSS (solid lines) from the data of the ascending portion of the *Aquarius* repeat swath that passes through the SPURS domain (see Fig. 2 for location). Correlation functions computed from ancillary SSS data are shown by the dashed lines. Different colors correspond to different latitude bands (see text for details). The ensemble-mean approximation by the Gaussian function with the *e*-folding scale of 90 km is shown by the heavy green line. (b) The corresponding wavenumber spectra (normalized) are shown.

Aquarius SSS, is that it fails to accommodate the negative (oscillatory) lobe of the sample correlation array. Although it is possible, in principle, to utilize a more sophisticated analytical function to fit the estimations, the simpler Gaussian model has been selected for the following reasons. First, one of the strict requirements on the choice of a possible analytical form of the correlation function in the OI analysis is that such a function must be positive definite; that is, the eigenvalues of each resulting correlation matrix must be nonnegative (Gandin 1965; Bretherton et al. 1976; Thiebaux and Pedder 1987; Weber and Talkner 1993). This is difficult to test for an arbitrary correlation model in two dimensions (Weber and Talkner 1993). In this regard, the correlation model given by the Gaussian function is proven to be positive definite on every Euclidian space and on the sphere (Yaglom 1986; Weber and Talkner 1993), which warrants stability of the algorithm. This choice may not be truly optimal; nonetheless it is suitable, since the decorrelation scales and the major structure of the observed correlations are well reproduced by the Gaussian model (see also the appendix). Second, interpolation with the Gaussian function can be considered as a general form of a low-pass filter acting on the data (McIntosh 1990; Sokolov and Rintoul 1999). Consideration of the assumptions used to compute correlations from the along-track satellite data suggests that such a low-pass filtration would be more preferable than the case of a bandpass filter, which would correspond to the oscillatory correlation model (Sokolov and Rintoul 1999). More sophisticated functional forms could be utilized when more precise data on the SSS correlation structure become available.

The analysis of along-track data gives some useful information about the characteristic meridional scales of SSS variability, but it tells us virtually nothing about the zonal scales. One way to overcome this problem is to assume that the spatial correlations are isotropic. This might be true in some areas but unlikely, for example, in the tropical region, where both atmospheric forcing and ocean dynamics are strongly anisotropic (Delcroix et al. 2005; Reverdin et al. 2007). Yet, limited information exists on the characteristic time and space scales of SSS variability in the ocean (Delcroix et al. 2005; Reverdin et al. 2007). Studying seasonal variability of SSS in the North Atlantic, Reverdin et al. (2007) found that in most regions outside of the equatorial belt, the zonal and meridional scales are comparable, while near the equator the zonal scales are ~1.5–2 times larger than the meridional scales.

To add to the realism of our OI analysis, we also assume that in the tropical region (0°–15°N) the zonal scales are larger than the meridional scales and modify (6) to take an anisotropic form

$$c(r_x, r_y) = \exp(-r_x^2/R_x^2 - r_y^2/R_y^2), \tag{7}$$

where r_x and r_y are spatial lags in the zonal and meridional directions, respectively; and R_x and R_y are the

TABLE 1. The variance and correlation length scales (the lag of the first zero crossing of the spatial correlation function) of mesoscale SSS variability as seen by *Aquarius* in 10° latitude bins in the North Atlantic.

Latitude band (°N)	Variance (psu^2)	Length scale (km)
0–10	0.249	150
10–20	0.046	160
20–30	0.023	135
30–40	0.079	140

associated zonal and meridional decorrelation scales. The meridional scale is set as $R_y = 90$ km (the same as in the subtropical region), while the zonal scale varies from $R_x = 180$ km at the equator to $R_x = 90$ km at 15°N as follows:

$$R_x(y) = 180\exp(-y^2/324.6)\,\text{km}, \quad 0° \le y \le 15°\text{N}, \quad (8)$$

where y is latitude in degrees. Near the equator, the aspect ratio R_x/R_y equals 2 (following Reverdin et al. 2007) and gradually decreases toward higher latitudes. At latitude 15°N, the correlation function (7) becomes isotropic ($R_x = R_y = 90$ km) and matches the correlation function given by (6). We note, however, that our assumptions of the zonal decorrelation scales are somewhat arbitrary due to the lack of appropriate high-resolution SSS data. (It has been determined a posteriori that the use of the anisotropic correlation in the tropics results in slight improvement of the OI SSS analysis.)

4) Error statistics

Analysis of *Aquarius* along-track SSS data (e.g., Fig. 3) reveals that there are long-wavelength errors (interbeam biases) that are correlated over long distances along the satellite tracks. To incorporate statistical information on these errors into our OI scheme, we adopt the idea that has originally been developed for altimeter applications (e.g., Blanc et al. 1995; Le Traon et al. 1998) and introduce the error covariance model for the *Aquarius* data in the form

$$\langle \varepsilon_i \varepsilon_j \rangle = \delta_{ij}\sigma_w^2 + \sigma_L^2 \quad \text{if data points } i,j \text{ are on the same track and beam and in the same cycle, and}$$

$$\langle \varepsilon_i \varepsilon_j \rangle = \delta_{ij}\sigma_w^2 \quad \text{otherwise},$$

where δ_{ij} is the Kronecker delta, σ_w^2 is the variance of the uncorrelated (white) noise, and σ_L^2 is the variance of the long-wavelength (along track) error.

Thus, the algorithm allows two types of random errors to contribute to the elements of the error covariance matrix: the white noise (diagonal elements), representing uncorrelated errors; and the long-wavelength error (off-diagonal elements), representing interbeam biases that correlate over long distances along the satellite tracks. Each beam is modeled as having independent errors.

Taking into account prior filtering of the along-track SSS, the variance of the white noise in the input data is assumed to be 10% of the signal variance, independent of the geographical location. It is thus assumed that uncorrelated errors, although relatively small, are still present in the data, allowing for some additional smoothing during the OI procedure.

The long-wavelength error in *Aquarius* observations of SSS is difficult to assess in a direct way due to the lack of a proper reference or "ground truth." To infer the statistical structure of the correlated portion of the retrieval error in *Aquarius* data, we compare statistics of the interbeam differences as seen by HYCOM (ancillary SSS) and those evaluated from *Aquarius* observations. In this way, we diminish the effects of large-scale biases that may simultaneously be present in both the *Aquarius* and HYCOM data.

The statistics of the interbeam differences are evaluated using *Aquarius* ground-track segments that span the entire domain from 0° to 40°N. To eliminate contributions from mesoscale SSS anomalies (Fig. 6), the along-track SSS data are low-pass filtered with a running Hanning filter of half-width of ~600 km. The interbeam differences are computed for each ground track as SSS of the middle beam (red lines in Fig. 2) minus SSS of the two other beams (green and blue lines in Fig. 2). The covariances of the interbeam differences are computed as a function of along-track separation and then averaged over all tracks to obtain the ensemble statistics. The ancillary SSS data are processed in exactly the same way. The estimation of the long-wavelength error statistics is accomplished by comparing the covariances of the interbeam differences for *Aquarius* and ancillary SSS.

Figure 7a shows covariances of the interbeam differences as a function of along-track separation distance for *Aquarius* (red) and HYCOM (blue) SSS. Notice that the variance of the *Aquarius* SSS interbeam differences is consistently larger than its HYCOM counterpart at all lags, presumably due to correlated errors in *Aquarius* SSS retrievals. Assuming that the interbeam differences in *Aquarius* and HYCOM data are not correlated, we can estimate the statistical structure of the long-wavelength retrieval error in *Aquarius* SSS data as the difference between the *Aquarius* and HYCOM interbeam difference covariances (black). The corresponding variance spectrum is shown in Fig. 7b (black).

Both the covariance function and the spectrum of the long-wavelength error demonstrate that this error has a complex spatial structure. The spectrum is red with more energy concentrated at longer wavelengths with no significant peaks. To obtain a functional form for the long-wavelength error correlation to use in the OI algorithm, we utilize a simple analytical model given by the exponential function of the form

$$C_L(l) = \sigma_L^2 \exp(-l/R_L), \quad (9)$$

where l is the along-track separation distance and $R_L = 500$ km is the exponential decay scale. The estimate of

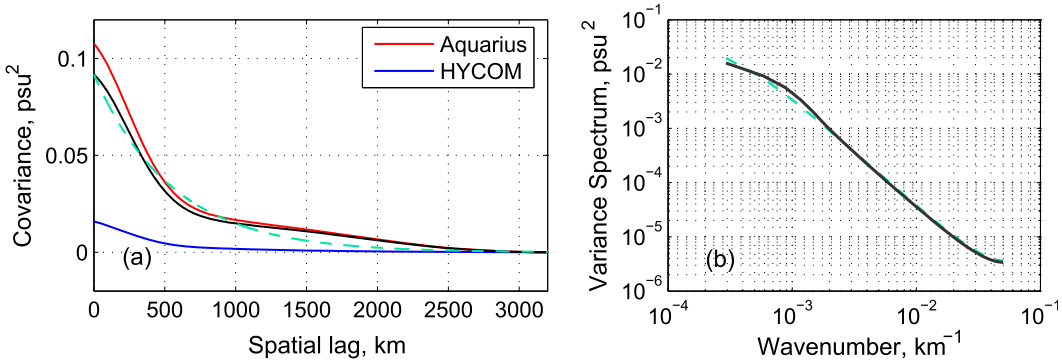

FIG. 7. (a) Autocovariances of interbeam differences computed from the data of the North Atlantic (0°–40°N). Red and blue curves represent *Aquarius* and ancillary SSS, respectively. The black curve is the difference between the two, representing the covariance of the long-wavelength error in *Aquarius* data. Its approximation by the exponential function is shown by the green dashed curve. (b) The associated spectra are shown.

R_L is obtained by fitting the curve (9) to the interbeam bias statistics, as shown in Fig. 7 by the green curve.

The model (9) is chosen to represent the error correlation structure because this is the simplest model consistent with the data. It provides a good fit to the error correlation array over the distance range 0–600 km over which the correlation is significant, and it satisfies the functional requirements of OI (Weber and Talkner 1993).

The variance of the long-wavelength error is assumed to be independent of the geographical location ($\sigma_L^2 \approx 0.085\,\mathrm{psu}^2$; Fig. 7a, black curve at zero spatial lag). However, the ratio of the error variance to the signal variance is allowed to vary with latitude, following the associated changes in the signal variance (Table 1). These variations are modeled as follows:

$$\eta = [1 - \exp(-y^2/225)]/1.43 + 0.3, \qquad (10)$$

where η is the ratio of the long-wavelength error variance to signal variance. Thus, the relative long-wavelength error variance varies from 30% in the near-equatorial region, where the signal variance is large, to about 100% at midlatitudes, where the signal variance is relatively low (Table 1).

5) IMPLEMENTATION

The OI SSS analysis is computed weekly on a 0.25° longitude × 0.25° latitude grid in the North Atlantic between 0° and 40°N, covering the period from September 2011 through August 2013. The weeks are defined to correspond to the standard level-3 product produced by ADPS. The OI SSS analysis is run in a local approximation; namely, only data points in a smaller subdomain around the analysis grid point are used. The radius of the subdomain is set to 600 km to accommodate the long-wavelength correlation structure (Fig. 7a). This approach seems to be reasonable. Data points beyond this radius contribute very little to the gridpoint analysis, since the decay length scales for both the signal and error are shorter than 600 km. The local approximation also helps to reduce effects of spatial inhomogeneity in the signal and error statistics (Weber and Talkner 1993). Finally, taking into account prior filtering of along-track SSS data and to reduce computational load, only one data point out of three (for each track/beam) is retained.

4. Mapping results

The following examples demonstrate the utility of the OI algorithm described above.

Figure 8 compares SSS maps in the North Atlantic for the week 26 August–1 September 2012 produced by three different analyses, including 1) the standard 7-day level-3 analysis currently produced by ADPS; 2) the conventional OI analysis (COI), which does not take into account the long-wavelength error ($\sigma_L^2 = 0$); and 3) the advanced OI scheme (AOI), which takes into account the long-wavelength error as discussed in section 3b(4). The standard 7-day level-3 product is constructed by bin averaging of *Aquarius* L2 SSS data within 1° longitude × 1° latitude spatial bins centered on a regular 1° resolution grid. The two OI analyses differ only in the way they treat the long-wavelength error; all other parameters are kept the same.

The bin-average procedure in the standard level-3 product effectively eliminates high-frequency (white) instrument noise. Yet, it fails to correct for correlated errors (interbeam biases) that manifest themselves as characteristic north–south-striped patterns aligned with the satellite tracks. These stripes are particularly visible when only ascending (Fig. 8a) or descending

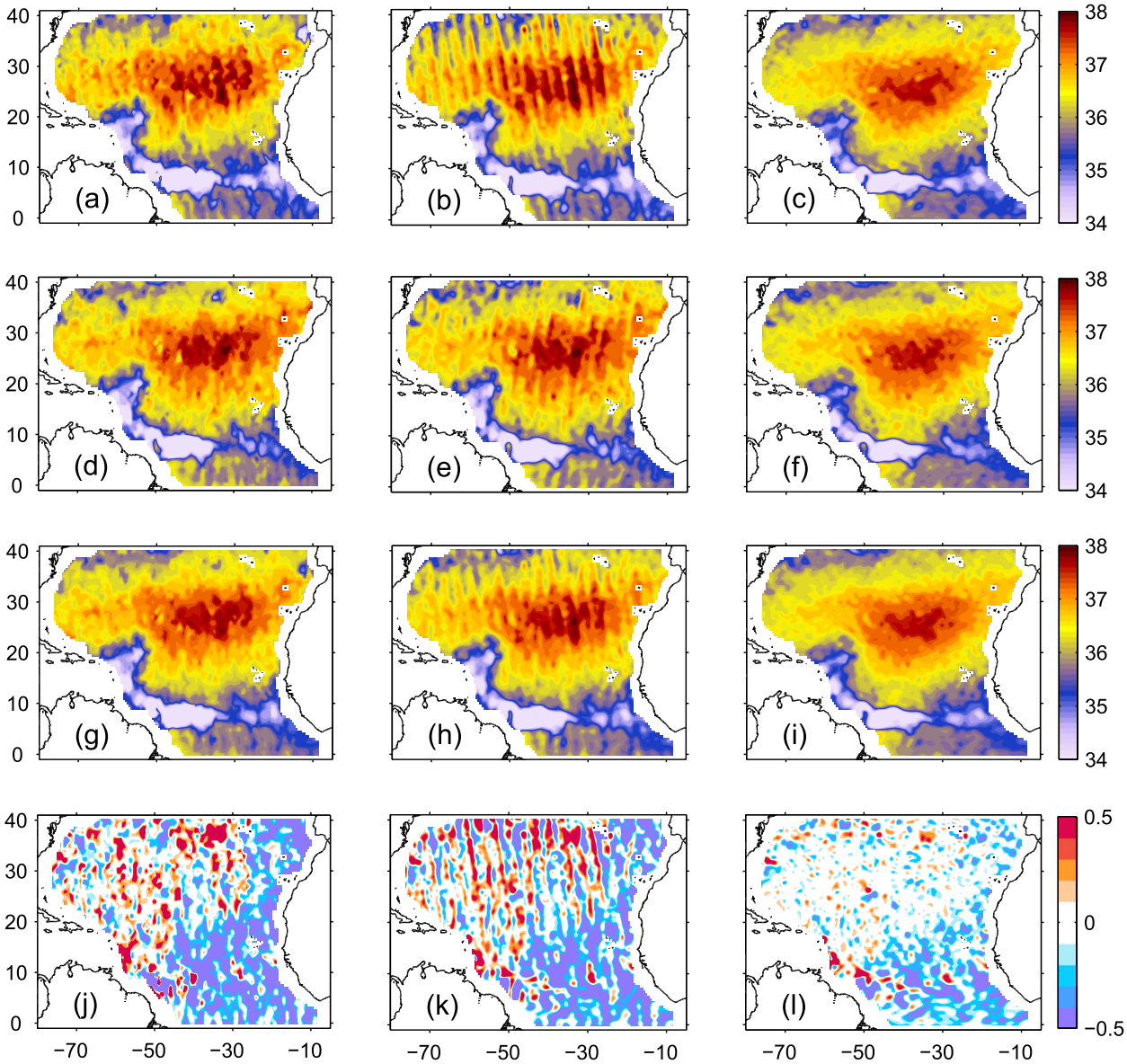

FIG. 8. Weekly SSS fields from *Aquarius* for the week 27 Aug–2 Sep 2012 constructed using different algorithms. (left) Bin averaging of *Aquarius* L2 SSS data within 1° longitude × 1° latitude bins centered on a regular 1° grid (standard 7-day level-3 product provided by ADPS; gaps in the maps are filled with linear interpolation). (middle) Conventional OI analysis (COI) that does not take into account long-wavelength errors ($\sigma_L^2 = 0$). (right) Advanced OI scheme (AOI) that takes into account long-wavelength errors. Upper row (a)–(c) Ascending data, (d)–(e) descending data, (g)–(i) ascending and descending combined, and (j)–(l) ascending minus descending.

(Fig. 8d) data are used as input data to construct the corresponding SSS maps, but they are also noticeable in the combined data (Fig. 8g). The same is true for the COI analysis. While resulting in better spatial resolution, the COI analysis leaves the long-wavelength error untreated, such that the satellite tracks appear even more visible in the corresponding SSS maps (Figs. 8b, 8e, and 8h). In contrast, the AOI scheme effectively eliminates the along-track correlated errors. The resulting SSS maps constructed from either ascending (Fig. 8c) or descending (Fig. 8f) data are nearly identical and both resemble the true ocean, free from spurious structures. The impact of taking into account the long-wavelength error in the AOI analysis is further illustrated by comparing the differences between the ascending and descending products (Figs. 8j–l). In the AOI analysis, these differences are significantly reduced.

The resolution capabilities as well as limitations of the AOI SSS analysis can be inferred from Fig. 9, which

compares the SSS map for the week 9–15 September 2012 with thermosalinograph (TSG) salinity measurements taken from 3-m depth by Research Vessel (R/V) *Thalassa*. The in situ measurements along the ship track reveal numerous small-scale structures with spatial scales smaller than the ~100-km *Aquarius* footprint. Not surprising, these structures are not resolved in the satellite-derived SSS map. At the same time, it is evident that the analysis is capable of capturing features at scales of at least 150 km (see also the appendix). An example is the tongue of low SSS at ~32°–33°N followed by the tongue of high SSS to the north (Fig. 9b). Unlike the TSG line, the SSS map from *Aquarius* provides a detailed two-dimensional view on the spatial structure of SSS variability in the region.

The high spatial resolution of weekly AOI SSS analyses is further illustrated by Fig. 10, which shows example SSS maps in the tropical North Atlantic for three weeks in July, September, and October 2012. Among the many features represented in Fig. 10 is the plume of low-salinity water that extends far offshore off the coast of South America. The plume is associated with the Amazon River outflow and is present seasonally during summer and fall and weakens or disappears in other months (Muller-Karger et al. 1988; Lentz 1995; Ffield 2007). The *Aquarius* SSS maps show a very detailed structure of the plume (Lagerloef 2012). Figure 10a shows how the plume starts to spread eastward into the North Atlantic in July 2012, presumably in the retroflection of the North Brazil Current (Muller-Karger et al. 1988; Lentz 1995). Over time, as the plume extends farther eastward, it becomes less continuous. However, the boundaries of the plume remain well defined and are characterized by strong SSS gradients.

Finally, to characterize SSS variability in the North Atlantic in one concise picture, Fig. 11 shows a time–latitude plot of SSS along the meridional section passing through the SPURS domain. The section coincides with the *Aquarius* track passing through the SPURS domain (heavy red line in Fig. 2 along the ascending pass). SSS values along the section are obtained by linear interpolation of weekly AOI SSS maps. The analysis demonstrates a consistent pattern of seasonal variability that is most pronounced in the tropical region. A narrow belt of low SSS, presumably associated with the intertropical convergence zone (ITCZ), migrates from the southernmost position near the equator in early spring to the northernmost position at about 8°N in winter. This structure also exhibits rapid temporal changes in some cases and is characterized by strong spatial gradients (see also Fig. 10). The weakest seasonal variability is observed in the subtropics, particularly in the area of the subtropical salinity maximum. The location of the salinity maximum slightly changes during the course of the year from ~26°N in fall–winter, when SSS also reaches its maximum, to ~24°N in late spring, generally consistent with the analysis of historical hydrographic data (A. Gordon 2013, personal communication).

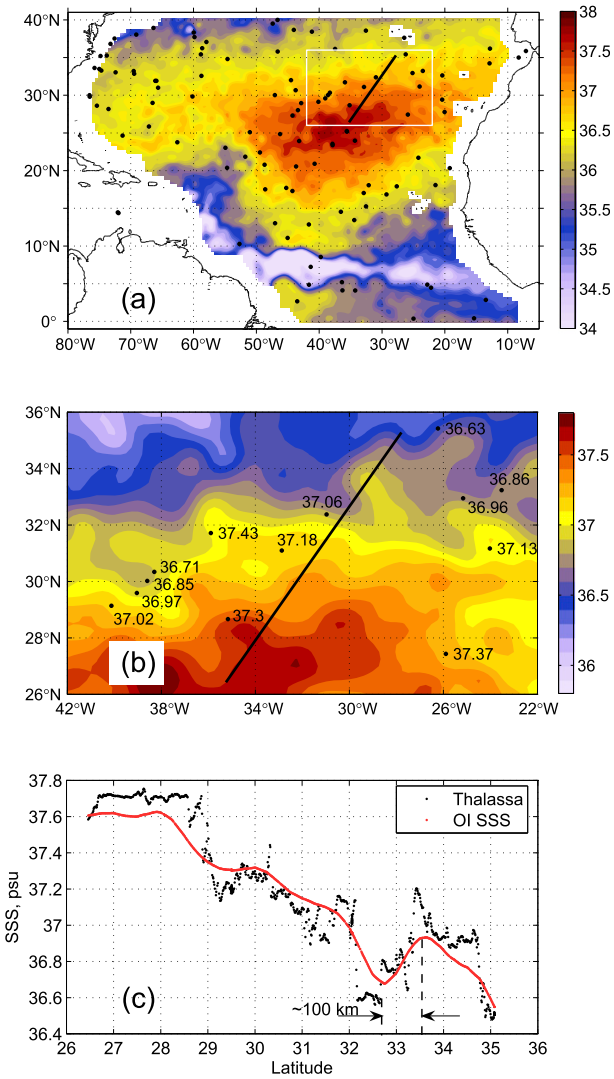

FIG. 9. (a) *Aquarius* AOI SSS (psu) for the week 9–15 Sep 2012. Dots show locations of Argo profiling floats surfaced during the same week. The black line shows locations of TSG measurements taken by R/V *Thalassa*. (b) As in (a), but zoomed in to the region 26°–36°N, 42°–22°W. Note that the color scales in (a) and (b) are different. (c) Comparison of AOI SSS map with TSG salinity measurements. The RMSD = 0.12 psu.

5. Verification statistics and intercomparison of SSS analyses

Argo buoy salinity measurements in the near-surface layer are used to provide OI error statistics during the

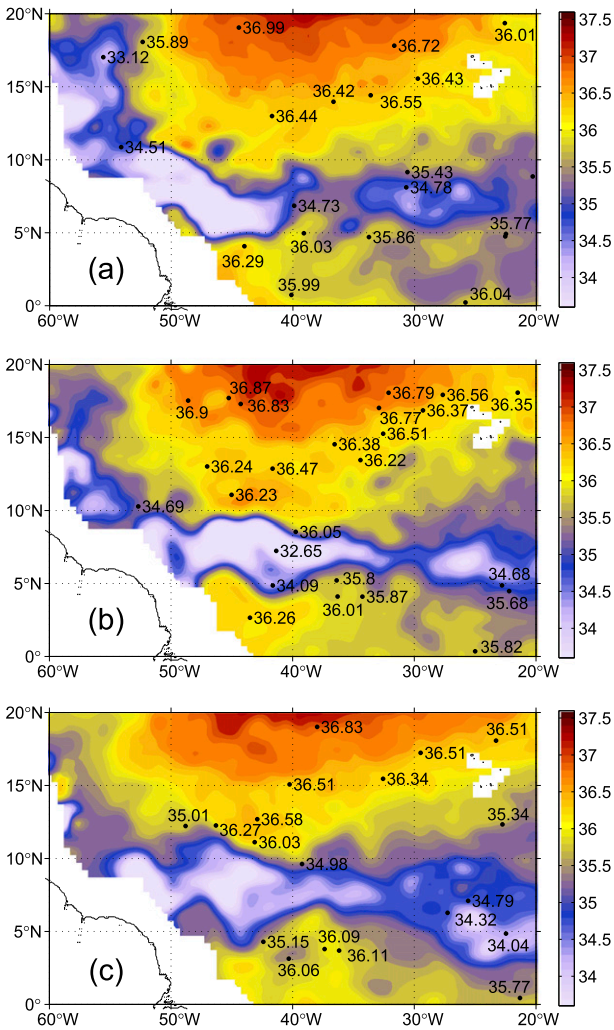

FIG. 10. *Aquarius* AOI SSS in the tropical North Atlantic for (a) 29 Jul–4 Aug 2012, (b) 9–15 Sep 2012, and (c) 21–27 Oct 2012. Black dots show locations of Argo buoy measurements for the corresponding week.

period from September 2011 through August 2013. The error statistics are calculated by comparing buoy measurements for a given week with SSS values at the same locations obtained by interpolating the corresponding *Aquarius* OI SSS maps. To quantify specifically the effect of incorporating error statistics into the OI algorithm, two versions of the OI analysis are run: AOI and COI. Also, in order to answer the question whether the OI analysis significantly improves the accuracy of *Aquarius*-derived SSS maps, the analysis-to-buoy comparisons are made for the standard level-3 SSS product currently produced by the ADPS.

The number of buoy data per each week in the North Atlantic is around 80 with quasi-random geographical distribution (e.g., Fig. 9a), and it remains around this number during the course of *Aquarius* measurements. The only exception is fall 2012, when a large number of Argo floats were deployed in the SPURS domain. The buoy data are typically drawn at 4–5-m depth and in most cases provide quite accurate representation of SSS. Under certain meteorological conditions, however, the difference between salinity at 5-m depth and the sea surface can be significant and exceed 0.1 psu (Henocq et al. 2010; Lagerloef et al. 2013).

Figure 12 compares different SSS analyses using common statistics. The mean average of the differences between each product and buoy data over all buoy locations, shown in Fig. 12a, is a measure of bias. A negative number in this case implies that on average the SSS estimate from *Aquarius* data is fresher than the Argo buoy data, and vice versa. The weekly time series of the root-mean-square differences (RMSD) between each of the analyses and buoy data are shown in Fig. 12b. Table 2 summarizes the mean, standard deviation, and RMSD of the differences between the analyses and buoy data for the 104-week period of comparison.

Several conclusions can be made from Fig. 12 and Table 2. First, the average biases for the three analyses are all smaller than 0.03 psu (Table 2). However, the weekly time series of the biases (Fig. 12a) reveal that there are periods, such as in the fall of 2011, when the biases are significant. For example, the COI analysis and the standard level-3 product are both ~0.08 psu fresher than the buoy data in October 2011 and ~0.1 psu saltier than the buoy data in January 2012. The AOI analysis results in much smaller biases, but it does not completely eliminate them. All three analyses exhibit periods of both negative and positive biases that tend to cancel each other over the 104-week period of comparison. In general, the standard deviation of the weekly biases is the smallest for the AOI analysis as compared to the other two analyses (Table 2).

The RMSD differ significantly for the three analyses. On average, the RMSD of the AOI analysis is about 35% less than that of the COI analysis and about 40% less than that of the standard level-3 product (Table 2). Figure 12b demonstrates that the AOI analysis has the lowest RMSD with respect to the buoy data for nearly all weeks. In all three analyses, the buoy-to-analysis comparison has the worst RMSD in spring and summer. This is likely a reflection of the fact that very shallow mixed layers are often formed in spring and summer, so that salinity at 4–5-m depth measured by a typical Argo buoy may differ from that at the sea surface. A detailed comparison (not shown here) indicates that multiple spikes in the RMSD time series, particularly in the standard level-3 product, are caused by a few buoys

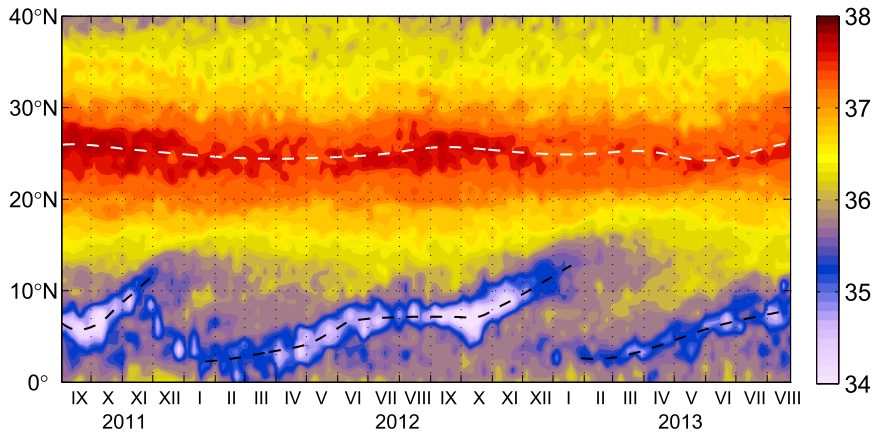

FIG. 11. Time–latitude plot of AOI SSS (psu) along the meridional section passing through the SPURS domain (the location of the section is shown by the heavy red line in Fig. 2 along the ascending satellite pass). The white dashed line approximates the location of the subtropical SSS maximum. The black dashed line approximates the seasonal march of the ITCZ.

located in the tropics. The fact that the spikes are observed in spring and summer suggests that these spikes are likely due to misrepresentation of SSS by the Argo buoy measurements, as discussed above. It is also important to note that the RMSD of the AOI analysis is smaller than 0.2 for nearly all weeks during the winter season when, due to surface cooling and usually stronger winds, mixing penetrates to greater depths; thus, buoy

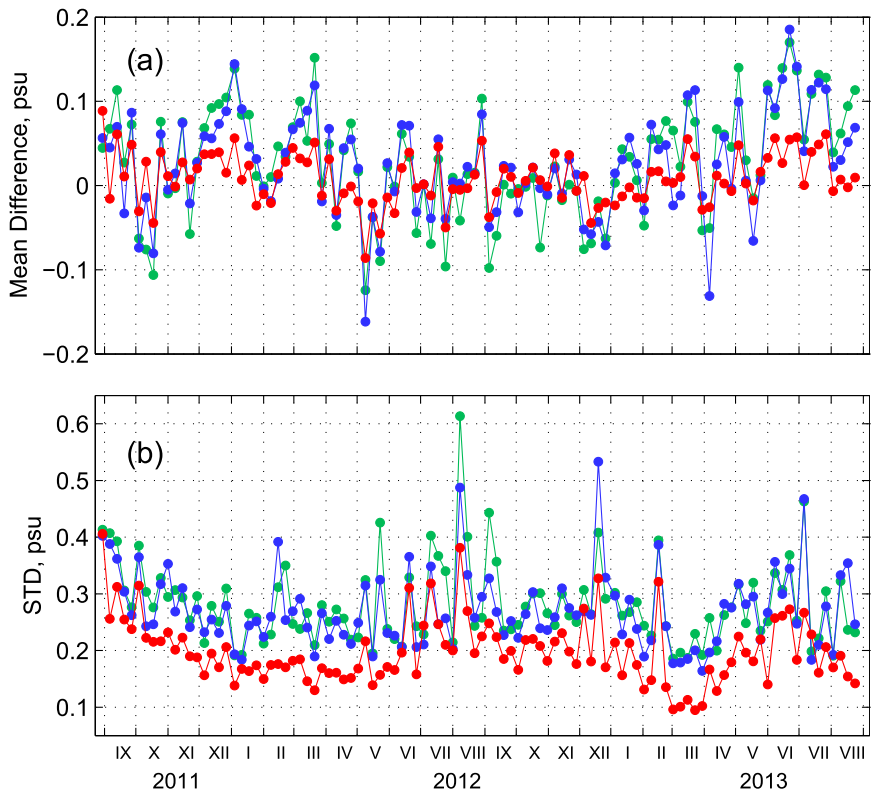

FIG. 12. (a) Weekly mean differences and (b) RMSD between Argo buoy data in the North Atlantic (0°–40°N) and three *Aquarius* SSS analyses: AOI (red), COI (blue), and level-3 SSS product provided by ADPS (green). The error statistics are computed by comparing Argo buoy measurements for a given week with SSS values at the same locations obtained by interpolation of the corresponding SSS maps.

TABLE 2. Biases and RMSD statistics between weekly satellite SSS analyses and buoy SSS in the North Atlantic for the period from September 2011 to August 2013.

Analysis	Mean bias (psu)	Std dev of the weekly biases (psu)	Mean RMSD (psu)
Level 3	0.028	0.065	0.282
COI	0.026	0.06	0.27
AOI	0.009	0.03	0.198

measurements at 4–5-m depth provide more accurate representation of SSS.

The utility of the AOI product is further illustrated by Fig. 13, which compares histograms of the differences between the buoy data in the North Atlantic (0°–40°N) and the three SSS analyses. The AOI estimates have an overall good agreement with the buoy data, such that the histogram of the differences is quite narrow, with ~55% of the differences falling into the range [−0.1, 0.1] psu. For comparison, this number is 36% for the COI analysis and about 34% for the standard level-3 product. The number of outliers, defined here as the differences larger than 0.5 psu, is about 3% in the AOI analysis, 5% in the COI analysis, and 6% in the standard level-3 product. One should keep in mind, however, that the relatively poor performance of the standard level-3 product with respect to the buoy data is partly due to the coarser grid on which the product is constructed.

Finally, Fig. 14 shows the scatterplots between the *Aquarius* SSS (mapped by the three analyses) and Argo buoy data, which clearly demonstrates where most of the close agreement between the AOI SSS analysis and in situ data is achieved. The scatter of points is considerably reduced over the regions where SSS is higher than ~35.5 psu (yellow-to-red colors in Fig. 5), but it remains significant over fresher areas, generally in the tropics (blue-to-magenta colors in Fig. 5). There are a few possible explanations for this effect. First, the tropics are characterized by vigorous variability at different space and time scales (Fig. 11), including small-scale variability. In the presence of strong spatial gradients (e.g., Fig. 10), the difference between a point measurement by a buoy and the area-averaged SSS sampled by *Aquarius* can exceed 0.2 psu (Lagerloef et al. 2010). Another source of discrepancy can be related to strong vertical gradients of salinity in the near-surface layer, such that salinity at 5-m depth, sampled by a typical Argo buoy, differs significantly from the surface salinity, sampled by *Aquarius*. Vertical salinity differences larger than 0.1 psu (sometimes as large as 1.0 psu) are often observed in the tropical belt between the equator and 15°N, which coincides with the average position of ITCZ (Henocq et al. 2010). It follows that the observed relatively large discrepancies between the *Aquarius* and buoy data in the tropics are not necessarily errors in *Aquarius* measurements or errors in the mapping procedure, but may rather reflect the disparity between time and space scales captured by two different observational platforms.

6. Summary and discussion

A method has been presented for mapping SSS fields from *Aquarius* level-2 data. The method is based on optimal interpolation (OI) and estimates SSS at a grid point as a weighted sum of nearby satellite observations with the weights optimized to minimize the estimation error variance. The key element of the proposed advanced OI (AOI) algorithm is that it takes into account statistics of correlated errors in the satellite retrievals, referred to here as interbeam biases that appear to correlate over long distances along the satellite tracks.

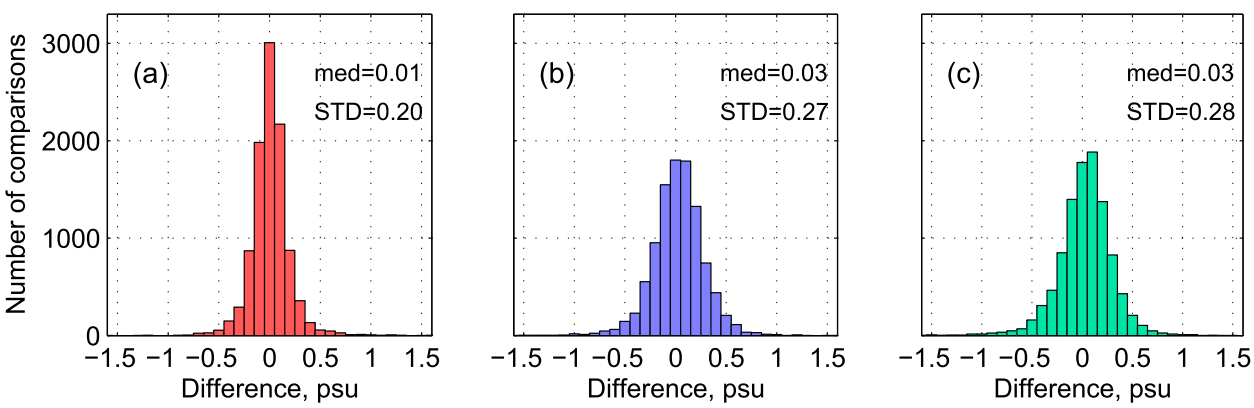

FIG. 13. Statistics of the differences between Argo buoy data in the North Atlantic (0°–40°N) and three *Aquarius* SSS analyses: (a) AOI, (b) COI, and (c) standard level-3 SSS product provided by ADPS. The error statistics are computed by comparing Argo buoy measurements for a given week with SSS values at the same locations obtained by interpolation of the corresponding *Aquarius* SSS maps.

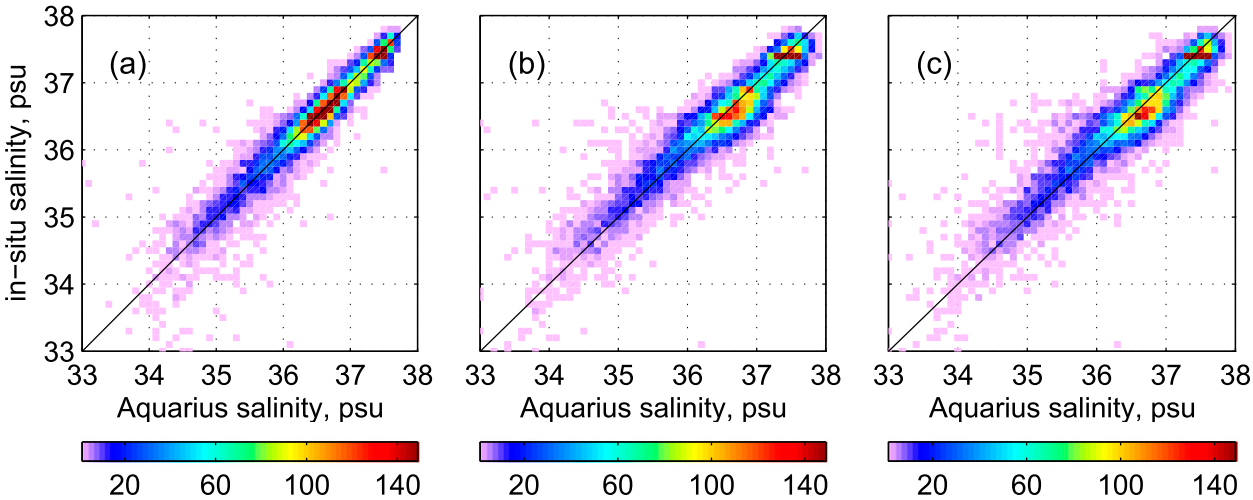

FIG. 14. Scatterplots of *Aquarius* weekly SSS analyses and collocated Argo buoy data in the North Atlantic (0°–40°N). The *Aquarius* SSS analyses are (a) AOI, (b) COI, and (c) standard level-3 SSS product provided by ADPS. Colors represent the number of points in 0.1-psu bins. The error statistics are computed by comparing Argo buoy measurements for a given week with SSS values at the same locations obtained by interpolation of the corresponding *Aquarius* SSS maps.

The inclusion of this type of error information into the AOI algorithm has been shown to result in more accurate SSS maps, free from spurious structures.

Examples have been presented that suggest that the OI technique can be an effective tool for mapping *Aquarius* SSS while correcting for various errors in the data. The quality of the AOI analysis has been demonstrated by considering the agreement between synoptic features in the SSS fields and those observed in independent in situ data, particularly high-resolution TSG data. The AOI analysis has been shown to resolve SSS features at scales of ~150 km and larger, consistent with the limited resolution of the input data, and to observe North Atlantic SSS with space and time resolution not available from the present global Argo array.

A trial AOI SSS analysis is produced in the North Atlantic (0°–40°N) on a uniform grid with 0.25° grid resolution and with a temporal resolution of one week. Statistical comparison of the AOI analysis with respect to the Argo buoy data demonstrates its superior performance as compared to the standard level-3 product currently produced by the NASA Goddard Space Flight Center's Aquarius Data Processing System (ADPS). In particular, the estimated error of the AOI analysis is ~40% smaller than that of the standard level-3 product.

It is worth emphasizing that the analysis presented in this paper is to a large extent experimental, focusing on a limited area in the North Atlantic. The results can be considered only "suboptimal" in the sense that the signal and error statistics, required by the analysis, are determined approximately. Many assumptions have been made, some of which are not fully justified. In particular, the analysis scheme described here assumes both homogeneity and stationarity of the signal and error statistics, which is certainly one of the weakest aspects of the analysis. This is particularly relevant to the error correlation matrix. The results indicate that incorporating error information into the mapping procedure has a dramatic effect on the quality of resulting SSS maps. Seasonal and geographical variations in the variance and/or length scales of the correlated errors in *Aquarius* SSS retrievals are likely very important factors to consider, but these are beyond the scope of the present paper and will be evaluated in future studies.

Users of *Aquarius* SSS data should also be aware that there are large-scale, space- and time-varying satellite biases relative to the in situ data in the present global products (Lagerloef et al. 2013). This problem seems to be not severe for the North Atlantic between 0° and 40°N (Fig. 12a), but it must be addressed in future global and regional analyses. Although the quality of *Aquarius* level-2 data will surely improve in future data versions as processing algorithms improve, the methodology presented in this paper should continue to provide value-added SSS products for regional, high-resolution studies.

Digital data of the weekly AOI SSS analysis in the North Atlantic are currently available online (at http://iprc.soest.hawaii.edu/users/oleg/oisss/atl/; weekly SSS beginning from September 2011).

Acknowledgments. This research was supported by the National Aeronautic and Space Administration (NASA) Ocean Salinity Science Team through Grants

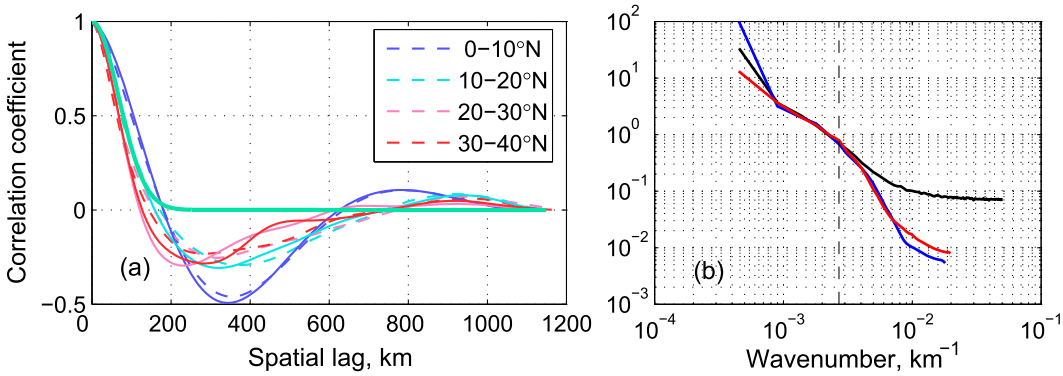

FIG. A1. (a) Solid lines show the ensemble-mean autocorrelations of AOI SSS for the ascending portion of the *Aquarius* repeat swath that passes through the SPURS domain (see Fig. 2 for location). Different colors correspond to different latitude bands. To compute these autocorrelations, weekly AOI SSS maps were interpolated into locations of actual satellite observations along the satellite track. For comparison, autocorrelations computed from the *Aquarius* L2 data [section 3b(3); Fig. 6] are reproduced here by the dashed lines. The green curve is the Gaussian function used in the AOI SSS analysis. (b) Zonal (red) and meridional (blue) wavenumber spectra of SSS computed from the 104 weekly AOI SSS fields in the region [15°–35°N, 50°–28°W]. The black line is the ensemble-mean spectrum derived from the *Aquarius* along-track measurements of SSS. All the spectra are normalized by the corresponding variance and scaled to have the same value at wavenumber $k = 2.2 \times 10^{-3}\,\mathrm{km}^{-1}$. The vertical dashed line corresponds to wavelength of 370 km.

NNX09AU75G and NNX12AK52G. Additional support was provided by the Japan Agency for Marine-Earth Science and Technology (JAMSTEC), by NASA through Grant NNX07AG53G, and by the National Oceanic and Atmospheric Administration through Grant NA17RJ1230 through its sponsorship of research activities at the International Pacific Research Center (IPRC). The Argo data were collected and made freely available by the International Argo Program and the national programs that contribute to it (http://www.argo.ucsd.edu). The Argo Program is part of the Global Ocean Observing System. The authors acknowledge the many constructive dialogues with members of the *Aquarius* calibration/validation team.

APPENDIX

Impact of Using the Simplified Correlation Model and Assessment of the Resolution Capability of the AOI SSS Analysis

To examine the effect of using the simplified correlation model for the AOI SSS analysis, we computed correlations of SSS anomalies using the data of weekly AOI SSS maps. To do this in a straightforward manner, the maps were interpolated into locations of actual observations along the satellite tracks. The SSS correlations were then computed in exactly the same way as using the original L2 data [section 3b(3)].

Figure A1 illustrates the ensemble-mean autocorrelations of AOI SSS for the repeat track shown by the heavy lines in Fig. 2. For comparison, autocorrelations computed from the *Aquarius* L2 data (Fig. 6) are shown by the dashed lines. The figure indicates that the shapes of the space-lagged correlation functions computed from the *Aquarius* along-track data agree well with those computed from the AOI output. This includes not only positive values prior to the first zero crossings (which are approximated by the Gaussian model) but also the negative lobes at larger lags. The mesoscale SSS variance, however, is much reduced in the AOI SSS fields as compared to the along-track data, consistent with the filtering properties of both the signal and error correlation models used in the analysis. The degree of reduction is about a factor of 1.5 in the tropics and up to 3 at higher latitudes.

To assess the spatial resolution capability of the AOI SSS analysis, we follow the spectral approach of Chelton et al. (2011) and compare wavenumber spectra of SSS evaluated from the gridded SSS product and the original *Aquarius* along-track SSS data. Figure A1b shows zonal (red line) and meridional (blue line) wavenumber spectra of SSS computed from the 104 weekly AOI SSS fields in the subtropical North Atlantic in the region extending from 15° to 35°N (2220 km × 2220 km) and from 50° to 28°W. The black line is the composite spectrum derived from the *Aquarius* along-track measurements of SSS. All the spectra are normalized by the variance and scaled to have the same value at wavenumber $k = 2.2 \times 10^{-3}\,\mathrm{km}^{-1}$ (wavelength = 450 km).

Figure A1b demonstrates that for wavenumbers smaller than about $2.7 \times 10^{-3}\,\mathrm{km}^{-1}$ (wavelengths larger

than about 370 km), the AOI and *Aquarius* level-2 SSS spectra are very similar in shape. In fact, the three curves are nearly indistinguishable for wavelengths between 450 and 1100 km. [Different spectral behavior at the largest scales is due to the area of the subtropical SSS maximum being elongated in the zonal direction (e.g., Fig. 5), so that the large-scale meridional gradients of SSS are larger than the zonal ones.] For wavenumbers higher than about $2.7 \times 10^{-3}\,\mathrm{km}^{-1}$, the AOI SSS spectra quickly roll off with increasing wavenumber, indicating the smoothing effect of the AOI procedure. It is thus apparent that the spatial resolution capability of the AOI SSS analysis is about 370–450 km in terms of a wavelength (scales larger than about 120 km), consistent with our estimates in section 4 (Fig. 9).

REFERENCES

Bingham, F. M., S. D. Howden, and C. J. Koblinsky, 2002: Sea surface salinity measurements in the historical database. *J. Geophys. Res.,* **107,** 8019, doi:10.1029/2000JC000767.

Blanc, F., P.-Y. Le Traon, and S. Houry, 1995: Reducing orbit error with an inverse method to estimate the oceanic variability from satellite altimetry. *J. Atmos. Oceanic Technol.,* **12,** 150–160, doi:10.1175/1520-0426(1995)012<0150:ROEFAB>2.0.CO;2.

Bretherton, F. P., R. E. Davis, and C. B. Fandry, 1976: A technique for objective analysis and design of oceanographic experiments applied to MODE-73. *Deep-Sea Res. Oceanogr. Abstr.,* **23,** 559–582, doi:10.1016/0011-7471(76)90001-2.

Chassignet, E. P., and Coauthors, 2009: U.S. GODAE: Global ocean prediction with the Hybrid Coordinate Ocean Model (HYCOM). *Oceanography,* **22,** 64–75, doi:10.5670/oceanog.2009.39.

Chelton, D. B., M. G. Schlax, and R. M. Samelson, 2011: Global observations of nonlinear mesoscale eddies. *Prog. Oceanogr.,* **91,** 167–216, doi:10.1016/j.pocean.2011.01.002.

Clancy, R. M., P. A. Phoebus, and K. D. Pollak, 1990: An operational global-scale ocean thermal analysis system. *J. Atmos. Oceanic Technol.,* **7,** 233–254, doi:10.1175/1520-0426(1990)007<0233:AOGSOT>2.0.CO;2.

Delcroix, T., M. J. McPhaden, A. Dessier, and Y. Gouriou, 2005: Time and space scales for sea surface salinity in the tropical ocean. *Deep-Sea Res. I,* **52,** 787–813, doi:10.1016/j.dsr.2004.11.012.

Ducet, N., P. Y. Le Traon, and G. Reverdin, 2000: Global high-resolution mapping of ocean circulation from TOPEX/Poseidon and ERS-1 and -2. *J. Geophys. Res.,* **105,** 19 477–18 498, doi:10.1029/2000JC900063.

Durack, P. J., and S. E. Wijffels, 2010: Fifty-year trends in global ocean salinities and their relationship to broad-scale warming. *J. Climate,* **23,** 4342–4362, doi:10.1175/2010JCLI3377.1.

Ffield, A., 2007: Amazon and Orinoco River plumes and NBC rings: Bystanders or participants in hurricane events? *J. Climate,* **20,** 316–333, doi:10.1175/JCLI3985.1.

Gandin, L. S., 1965: *Objective Analysis of Meteorological Fields.* Israel Program for Scientific Translations, 242 pp.

Gouretski, V. V., and K. P. Koltermann, 2007: How much is the ocean really warming? *Geophys. Res. Lett.,* **34,** L01610, doi:10.1029/2006GL027834.

Henocq, C., J. Boutin, F. Petitcolin, G. Reverdin, S. Arnault, and P. Lattes, 2010: Vertical variability of near-surface salinity in the tropics: Consequences for L-band radiometer calibration and validation. *J. Atmos. Oceanic Technol.,* **27,** 192–209, doi:10.1175/2009JTECHO670.1.

Lagerloef, G., 2012: Satellite mission monitors ocean surface salinity. *Eos, Trans. Amer. Geophys. Union,* **93,** 233–234, doi:10.1029/2012EO250001.

——, and Coauthors, 2008: The Aquarius/SAC-D mission: Designed to meet the salinity remote-sensing challenge. *Oceanography,* **21,** 68–81, doi:10.5670/oceanog.2008.68.

——, and Coauthors, 2010: Resolving the global surface salinity field and variability by blending satellite and in situ observations. *Proceedings of OceanObs'09: Sustained Ocean Observations and Information for Society,* J. Hall, D. E. Harrison, and D. Stammer, Eds., Vol. 2, ESA Publ. WPP-306, doi:10.5270/OceanObs09.cwp.51.

——, and Coauthors, 2013: Aquarius salinity validation analysis. JPL Aquarius Project Doc. AQ-014-PS-0016, Data Version 2.0, 36 pp. [Available online at ftp://podaac-ftp.jpl.nasa.gov/allData/aquarius/docs/v2/AQ-014-PS-0016_AquariusSalinityDataValidationAnalysis_DatasetVersion2.0.pdf.]

Lentz, S. J., 1995: Seasonal variations in the horizontal structure of the Amazon plume inferred from historical hydrographic data. *J. Geophys. Res.,* **100,** 2391–2400, doi:10.1029/94JC01847.

Le Traon, P. Y., F. Nadal, and N. Ducet, 1998: An improved mapping method of multisatellite altimeter data. *J. Atmos. Oceanic Technol.,* **15,** 522–534, doi:10.1175/1520-0426(1998)015<0522:AIMMOM>2.0.CO;2.

Le Vine, D. M., G. S. E. Lagerloef, F. R. Colomb, S. H. Yueh, and F. A. Pellerano, 2007: Aquarius: An instrument to monitor sea surface salinity from space. *IEEE Trans. Geosci. Remote Sens.,* **45,** 2040–2050, doi:10.1109/TGRS.2007.898092.

McIntosh, P. C., 1990: Oceanographic data interpolation: Objective analysis and splines. *J. Geophys. Res.,* **95,** 13 529–13 542, doi:10.1029/JC095iC08p13529.

Muller-Karger, F. E., C. R. McClain, and P. L. Richardson, 1988: The dispersal of the Amazon's water. *Nature,* **333,** 56–58, doi:10.1038/333056a0.

Reverdin, G., E. Kestenare, C. Frankignoul, and T. Delcroix, 2007: Surface salinity in the Atlantic Ocean (30°S–50°N). *Prog. Oceanogr.,* **73,** 311–340, doi:10.1016/j.pocean.2006.11.004.

Reynolds, R. W., and T. M. Smith, 1994: Improved global sea surface temperature analyses using optimal interpolation. *J. Climate,* **7,** 929–948, doi:10.1175/1520-0442(1994)007<0929:IGSSTA>2.0.CO;2.

——, ——, C. Liu, D. B. Chelton, K. S. Casey, and M. Schlax, 2007: Daily high-resolution-blended analyses for sea surface temperature. *J. Climate,* **20,** 5473–5496, doi:10.1175/2007JCLI1824.1.

Roemmich, D., and J. Gilson, 2009: The 2004–2008 mean and annual cycle of temperature, salinity, and steric height in the global ocean from the Argo program. *Prog. Oceanogr.,* **82,** 81–100, doi:10.1016/j.pocean.2009.03.004.

Sokolov, S., and S. R. Rintoul, 1999: Some remarks on interpolation of nonstationary oceanographic fields. *J. Atmos. Oceanic Technol.,* **16,** 1434–1449, doi:10.1175/1520-0426(1999)016<1434:SROION>2.0.CO;2.

Thiebaux, H. J., and M. A. Pedder, 1987: *Spatial Objective Analysis: With Applications in Atmospheric Science*. Academic Press, 299 pp.

——, E. Rogers, W. Wang, and B. Katz, 2003: A new high-resolution blended real-time global sea surface temperature analysis. *Bull. Amer. Meteor. Soc.,* **84,** 645–656, doi:10.1175/BAMS-84-5-645.

U.S. CLIVAR Office, 2007: Report of the U.S. CLIVAR Salinity Science Working Group. U.S. CLIVAR Rep. 2007-1, 46 pp. [Available online at http://www.usclivar.org/sites/default/files/Salinity_final_report.pdf.]

Weber, R. O., and P. Talkner, 1993: Some remarks on spatial correlation function models. *Mon. Wea. Rev.,* **121,** 2611–2617, doi:10.1175/1520-0493(1993)121<2611:SROSCF>2.0.CO;2.

Yaglom, A. M., 1986: *Correlation Theory of Stationary and Related Random Functions I. Basic Results*. Springer-Verlag, 526 pp.